Textile & Leather Review

ISSN 2623-6281| www.tlr-journal.com | 10.31881/TLR

# AGB-RRT*: An Anisotropic Gradient-guided and Flow-adaptive Path Planning Algorithm for UUVs in Complex 3D Environments

Yuchen Yang

**How to cite:** Yang Y. AGB-RRT*: An Anisotropic Gradient-guided and Flow-adaptive Path Planning Algorithm for UUVs in Complex 3D Environments. Textile & Leather Review. 2026; 9 *4339-4370* *https://doi.org/10.31881/TLR.2026.4339*

**How to link:** *https://doi.org/10.31881/TLR.2026.4339*

**Published:** 25 April 2026

# AGB-RRT*: An Anisotropic Gradient-guided and Flow-adaptive Path Planning Algorithm for UUVs in Complex 3D Environments

**Yuchen Yang**

School of Science, Nanjing University of Posts and Telecommunications, Nanjing, China

b23090406@njupt.edu.cn

**Article**

*https://doi.org/10.31881/TLR.2026.4339*

*Published 25 April 2026*

**ABSTRACT**

*The path-planning problem for unmanned underwater vehicles (UUVs) in long-endurance deep-sea missions is investigated, with a focus on the trade-off between navigation safety and energy efficiency. A novel AGB-RRT* algorithm is proposed to address these challenges within complex 3D environments. By leveraging the passive hydrostatic restoring characteristics of UUVs, a simplified 4-DOF planning model is established, and an energy-evaluation function is subsequently derived from fluid resistance theory. A terrain-guided "logical grid" heuristic is designed to enhance search efficiency. A probabilistic hybrid sampling strategy is further introduced to balance gradient-guided expansion with random exploration, which accelerates convergence while effectively avoiding local minima. The cost function integrates a flow-adaptive mechanism to prioritize energy-saving trajectories, while 3rd-order B-spline interpolation is applied to ensure curvature-continuous paths that satisfy kinematic requirements. The effectiveness of the AGB-RRT* algorithm is validated through simulations using real seabed bathymetry and vortex models. Results demonstrate that the proposed method significantly reduces both energy consumption and path length compared to standard RRT* and Informed-RRT*, providing a robust and practical solution for the autonomous navigation of UUVs in challenging underwater environments.*

**KEYWORDS**

*unmanned underwater vehicles, path planning, anisotropic sampling, flow-adaptive mechanism, 3rd-order B-spline smoothing*

## INTRODUCTION

Unmanned underwater vehicles (UUVs) have emerged as indispensable technological assets for maritime operations such as underwater pipeline inspection. The autonomy of these vehicles enables them to penetrate high-risk zones for long-endurance tasks, including marine environmental monitoring and search-and-rescue operations [1]. Recent integration of high-precision sensors, such as Doppler Velocity Logs, has significantly enhanced the 3D localization capabilities of UUVs [2]. Despite these technical advancements, ensuring robust obstacle avoidance and path planning within complex, unstructured 3D environments remains a focal point of current academic research [3]. Effective path planning can account for environmental complexity while deeply incorporating the physical kinematic constraints of the UUV to ensure that the generated trajectories are dynamically feasible. The substantial discrepancy between idealised geometric trajectories and practical underwater manoeuvres necessitates the development of advanced planning frameworks that unify the two.

The fundamental challenge of 3D path planning stems from the inherent conflict between operational efficiency and navigational safety. Minimizing path length is vital for extending the operational radius of UUVs with constrained battery capacities [4], while obstacle avoidance strategies in 3D space directly dictate the survivability of the vehicle [5]. This multi-objective optimization problem becomes particularly pronounced under intense dynamic disturbances [6]. Traditional planning methods often overlook the non-linear impact of ocean current velocity on UUV propulsion energy consumption. In regions with dramatic topographical variations, such as deep-sea trenches, a purely geometric shortest path frequently results in excessive energy dissipation [7]. Furthermore, the 3D maneuverability of UUVs is strictly governed by non-holonomic constraints, notably the unique physical attribute of "separation between the centers of gravity and buoyancy" [8]. Although existing studies have attempted to establish comprehensive risk assessment frameworks, most models remain inadequate in capturing the deep interaction between the UUV and its dynamic environment. Table 1 compares the planning objectives of typical existing studies with those of the work proposed in this paper.

Table 1. Comparison of planning objectives between typical studies and the proposed method.

| References | Route length | Energy/Risk | Multi-objects | Core Method |
|---|---|---|---|---|
| [1] | √ | × | × | Hybrid A* & APF Algorithm |

| | | | | |
|---|---|---|---|---|
| [2] | √ | × | × | Improved RRT (Cylindrical Sampling) |
| [3] | √ | √ | × | Time-Saving Path Planning |
| This paper | √ | √ | √ | Gradient-guided AGB-RRT* Algorithm |

Various meta-heuristic algorithms have been proposed to address search efficiency challenges in high-dimensional spaces. The Artificial Potential Field (APF) method is widely adopted for real-time obstacle avoidance due to its computational efficiency [9], although it remains prone to being trapped in local minima within U-shaped terrains. As a classic improved version of RRT, the Goal-biased RRT algorithm introduces a heuristic sampling probability toward the goal point to accelerate convergence, but its path quality is still limited by inherent randomness, resulting in low smoothness and poor stability in complex flow fields. The sampling-based Rapidly-exploring Random Tree Star (RRT*) algorithm, characterized by probabilistic completeness, serves as a robust tool for 3D path planning [10]. Nevertheless, the uniform sampling approach of RRT* often leads to slow convergence within vast deep-sea search spaces [11]. While integrating Particle Swarm Optimization [12] or Ant Colony Optimization [13] has improved search quality, these hybrid algorithms still suffer from severe sampling efficiency issues in narrow channels [14]. The sharp increase in computational complexity further limits their real-time performance in embedded control systems [15].

Deep Reinforcement Learning (DRL) provides a novel paradigm for managing dynamic underwater uncertainties, enabling agents to learn navigation strategies through environmental interaction [16]. Deep Q-Networks have demonstrated remarkable adaptability in UUV path planning within discrete action spaces [17]. The 3D path planning method proposed by Hao et al. [18] integrated an adaptive potential field with DRL to improve sample efficiency. Despite these advancements, reinforcement learning still faces drawbacks in high-dimensional continuous state spaces, including prolonged training cycles and excessive dependence on reward function design [19, 20]. The generated action sequences often lack necessary smoothness, causing frequent chattering of UUV thrusters [21]. The generalization capability of DRL models in unseen extreme terrains also remains to be further validated [22]. Such limitations in both stochastic sampling and model-free learning necessitate the exploration of hybrid mechanisms that incorporate physical principles of the environment.

The deep integration of physical field gradient information with stochastic sampling mechanisms has emerged as a prominent trend to balance the respective strengths of the aforementioned algorithms [23].

Gradient guidance allows the expansion of the random tree to achieve explicit physical directivity [24], creating a synergy that compensates for individual algorithm deficiencies under dynamic disturbances [25]. Existing methods, however, still struggle to simultaneously ensure path safety and energy efficiency in highly disturbed environments. Research gaps persist in achieving "stealthy current avoidance" while satisfying nonholonomic continuous constraints [26]. To fill these gaps, this paper introduces an AGB-RRT* algorithm that integrates gradient guidance and flow adaptation. Table 2 presents a comparison of contributions between this work and relevant literature.

Table 2. Comparison of contributions in the literature review.

| References | Risk/Energy Awareness | Real Terrain Data | Anisotropic Constraints | Kinematic Continuity | Core Fusion Mechanism |
|---|---|---|---|---|---|
| [18] | √ | √ | × | Reward-guided | APF + Deep Reinforcement Learning |
| [21] | √ | × | × | Prioritized Replay | DRL with Ocean Currents |
| [23] | √ | × | × | Path Pruning | Constrained Bi-RRT*-Smart |
| [24] | × | √ | × | Step-size Smoothing | Traditional APF + Modified RRT |
| This paper | √ | √ | √ | 3rd-order B-spline | Gradient-guided + Anisotropic Sampling |

The main contributions of this paper are summarised as follows:

A dynamic energy evaluation model is established by considering the 4-DOF physical characteristics of UUVs, non-linear drag resistance and Lamb-Oseen vortices;

An anisotropic ellipsoidal sampling mechanism modulated by environmental potential-field gradients is designed to overcome the sampling success rate bottleneck in narrow, deep-sea channels.

A flow-adaptive cost function is redefined to guide the UUV toward energy-efficient planning by avoiding adverse currents and exploiting favourable ones, with 3rd-order B-spline technology employed to ensure trajectory smoothness.

## PROBLEM FORMULATION AND SYSTEM MODELLING

During long-endurance deep-sea cruising missions, the motion characteristics of UUVs are subject to the intensive coupling of high-dimensional non-linear hydrodynamics and complex time-varying currents. To assess the engineering feasibility of trajectories generated by path-planning algorithms, a 6-DOF (six-degree-of-freedom) spatial motion model incorporating added mass and nonlinear damping coefficients is first established based on rigid-body dynamics. Given the prominent passive hydrostatic restoring characteristics arising from the separation of gravity and buoyancy centres in deep-sea scenarios, this representation is simplified to a 4-DOF planning model (3D coordinates and heading angle) via dimensional mapping. This simplification is primarily applicable to steady-state cruising, where substantial restoring torque constrains pitch and roll oscillations, while the flow-adaptive cost function in the proposed algorithm effectively compensates for the resulting deviations due to neglected high-frequency attitude coupling. This approach significantly enhances computational efficiency while maintaining the rigour of hydrodynamic constraints, providing sufficient fidelity for macroscopic energy optimisation even in strong flow fields. The subsequent derivation of an intrinsic energy consumption evaluation function is based on non-linear drag theory. Furthermore, a high-fidelity virtual environment—featuring complex terrain and non-uniform current fields—is reconstructed from GEBCO bathymetric data and Lamb-Oseen vortex models, thereby providing stringent, realistic physical boundaries for verifying the AGB-RRT* algorithm. Figure 1 illustrates the overall flowchart of this study.

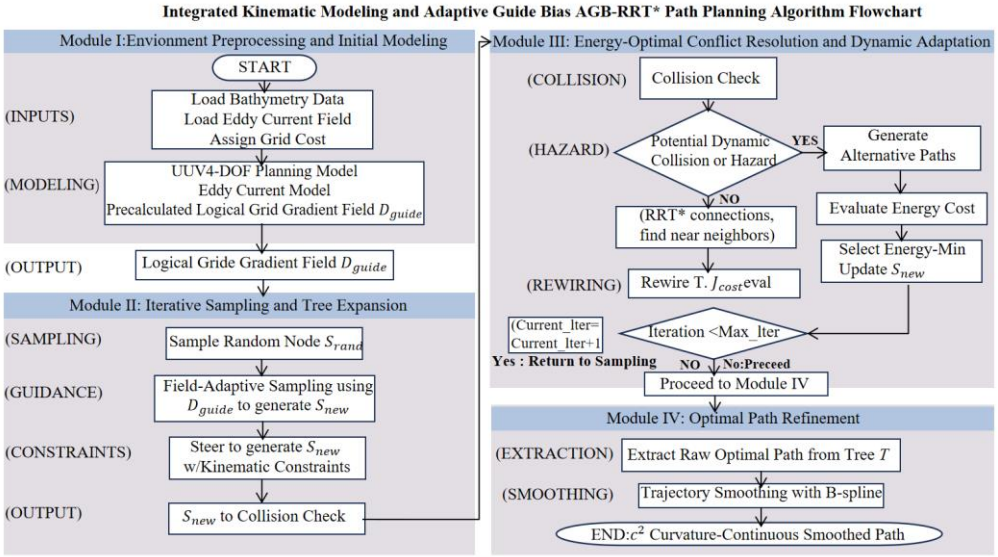


Figure 1. Overall flowchart of the proposed AGB-RRT* path planning framework

**Dimension Reduction Description of Kinematic State Space**

To accurately describe the pose evolution of a UUV in a 3D underwater space, this paper defines two orthogonal reference coordinate systems: The first is the Earth-fixed inertial coordinate system $\{E\}-OXYZ$, fixed to the sea surface, which is used to describe the UUV's global navigation position and absolute heading; The second is the body-fixed coordinate system $\{B\}-oxyz$, rigidly attached to the geometric buoyancy centre of the UUV, which is used to describe the relative velocity, acceleration, and force conditions of the vehicle itself. The generalised position vector η and velocity vector v of the UUV are defined as follows:

$$\eta=[x,y,z,\phi,\theta,\psi]^T,\nu=[u,v,w,p,q,r]^T \tag{1}$$

where $(x,y,z)$ are the 3D position coordinates in the inertial frame; $(\phi,\theta,\psi)$ are the roll angle, pitch angle, and yaw angle, respectively; $(u,v,w)$ are the linear velocities along the body's surge, sway, and heave directions; $(p,q,r)$ are the angular velocities rotating about each axis of the body.

In practical deep-sea engineering applications, long-endurance cruising-class UUVs usually follow the "separation of gravity and buoyancy centres" principle in structural design. Specifically, ballast adjustment is used to position the centre of gravity well below the centre of buoyancy, thereby achieving a large metacentric height. This physical design endows the UUV with a substantial passive hydrostatic restoring moment, enabling it to automatically return to a horizontal attitude after being disturbed by waves or currents. Therefore, at the path-planning decision-making level, we can reasonably ignore high-frequency attitude fluctuations and assume that its roll angle and pitch angle are self-stabilised (i.e.,). Furthermore, considering that most UUVs with a revolved-body configuration are underactuated systems lacking lateral thrusters, their sideslip velocity v is typically much smaller than the longitudinal propulsion velocity $u$ and can be approximated as zero.

A 4-DOF kinematic planning model is adopted to balance computational efficiency with physical realism for long-endurance missions. This simplified model serves the specific purpose of macroscopic global path planning rather than high-frequency attitude control. The AGB-RRT* algorithm focuses on generating spatially safe and energy-efficient waypoints, rendering a full 6-DOF model unnecessary at the global planning stage. Emphasis is placed on long-distance trajectory optimization, whereas fine attitude adjustments are handled

by lower-level control systems. This hierarchical framework significantly reduces the state-space dimensionality, facilitating efficient searches across extensive operational areas.

Based on the above physical facts and engineering assumptions, the state space at the planning level can be dimensionally reduced from a complex 6-DOF model [18] to a 4-DOF model, which significantly reduces the computational dimension while ensuring accuracy. According to the principle of rigid-body coordinate transformation, the kinematic equations in the inertial frame are expanded as:

$$\begin{cases} \dot{x} = u\cos\psi\cos\theta - v\sin\psi + w\sin\theta\cos\psi \\ \dot{y} = u\sin\psi\cos\theta + v\cos\psi + w\sin\theta\sin\psi \\ \dot{z} = -u\sin\theta + w\cos\theta \\ \dot{\psi} = r/\cos\theta \end{cases} \tag{2}$$

For the UUV's long-range near-horizontal cruise mission considered in this study, the roll angle $\phi$ and pitch angle $\theta$ are inherently self-stabilised by the passive hydrostatic restoring moment, and their fluctuations are extremely small. By introducing the small-angle assumption (i.e., $\phi \approx 0$, $\theta \approx 0$), the nonlinear coupling terms related to vertical attitude in the full 6-DOF kinematic equations are neglected, and the model is further linearised. Considering the underactuated characteristics of the UUV, the sideslip velocity $v$ is also neglected. The simplified 4-DOF kinematic model, which only retains the yaw rotation, is thus established as shown in Equation (3):

$$\dot{\eta}_{plan} = R(\psi)\cdot v_{plan} = \begin{bmatrix} \cos\psi & 0 & 0 \\ \sin\psi & 0 & 0 \\ 0 & 1 & 0 \\ 0 & 0 & 1 \end{bmatrix} \begin{bmatrix} u \\ w \\ r \end{bmatrix} \tag{3}$$

This equation not only describes the law of position update but also clarifies the non-holonomic constraint characteristic of the UUV: the UUV's instantaneous velocity must align with its body's longitudinal axis, and direct lateral translation, as possible for omnidirectional mobile robots, is not feasible. Figure 2 shows the schematic diagram of model dimension reduction from 6-DOF to 4-DOF.

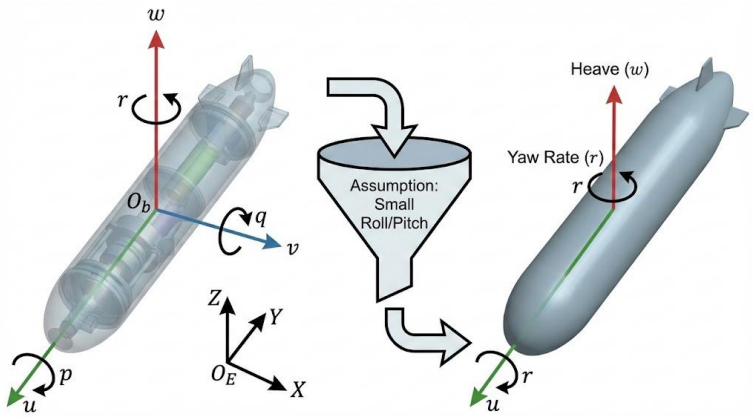


Figure 2. Schematic diagram of model dimension reduction

**Dynamic Equations with Fluid Damping**

In the high-density fluid environment of the deep sea, the motion of a UUV is not a simple geometric displacement, but is governed by the equilibrium of forces. Among these, hydrodynamic drag is the key factor determining energy consumption. Let the current velocity in the inertial frame be $V_c = [u_c, v_c, w_c]^T$, then the velocity of the UUV relative to the fluid, $v_r$, is given by:

$$v_r = v - R_E^B V_c \tag{4}$$

Based on Fossen's modeling theory for underwater robots [27], a dynamic equilibrium equation including full hydrodynamic coefficients is established:

$$M\dot{v} + C(v)v + D(v_r)v_r + g(\eta) = \tau \tag{5}$$

Where $g(\eta)$ is the restoring moment vector generated by gravity and buoyancy, and $\tau$ is the control force vector produced by the thrusters.

*Decomposition of the Inertia Matrix* $M$

The inertial properties of underwater rigid bodies differ from those on land, and the fluid carry-over effect must be considered. The inertia matrix $M$ is the superposition of the rigid-body mass $M_{RB}$ and the fluid added mass $M_A$:

$$M = M_{RB} + M_A = diag\{m - X_{\dot{u}}, m - Y_{\dot{v}}, m - Z_{\dot{w}}, I_z - N_{\dot{r}}\} \tag{6}$$

Where $m$ is the mass of the UUV, $I_z$ is the moment of inertia about the z-axis; $X_{\dot{u}}$, etc., are added mass coefficients that reflect the extra kinetic energy consumed by the UUV during acceleration and the pushing of the surrounding fluid.

*Nonlinear Hydrodynamic Damping* $D(v_r)$

It serves as the basis for energy consumption calculations and is the fundamental reason for considering flow-field factors in path planning. Considering both surface friction at low speeds and pressure drag at high speeds, the damping matrix is modelled as:

$$D(v_r) = D_L + D_Q(v_r) \tag{7}$$

Expanding the key longitudinal damping term $X_{drag}$, a strong nonlinear relationship between drag and relative velocity is observed:

$$X_{drag} = -(X_u + X_{u|u|}|u_r|)u_r \tag{8}$$

Where $X_u$ is the linear damping coefficient, and $X_{u|u|}$ is the quadratic vortex-induced damping coefficient. Further derivation of the instantaneous power $P_{prop}$ is required for the thruster to overcome the drag yields:

$$P_{prop} = F_{drag} \cdot u \approx k \cdot |u - u_c|^2 \cdot u \tag{9}$$

Where $k > 0$ is a positive proportionality coefficient that reflects the nonlinear relationship between relative velocity and propulsion power.

Equation (9) profoundly reveals the mechanism of "energy-assisted navigation"—When $u_c > 0$ (downstream), the relative velocity decreases, and the propulsion power drops cubically, resulting in "energy-saving gliding". When navigating upstream, the relative velocity increases, and the energy consumption surges exponentially. This physical characteristic indicates that the shortest path alone often implies an extremely high energy cost in the deep sea. This nonlinear relationship between the flow field and energy consumption provides a key theoretical basis for optimising the path-planning cost function.

**Mathematical Reconstruction of Complex Environmental Fields**

To construct a highly realistic simulation environment, this paper abandons the simplified practice of traditional algorithms that use regular geometric bodies (such as spheres and cylinders) to model obstacles, and adopts a data-driven environmental reconstruction strategy instead.

*Obstacle Risk Potential Field*

The global high-resolution bathymetry data released by GEBCO 2024[1] is adopted as the environmental input, and the bilinear interpolation algorithm is used to smooth the discrete grid data, reconstructing a continuously differentiable seabed height surface $H(x,y)$ To quantify the collision threat of terrain to the UUV, a safety threshold $\rho_0$ is defined, and the obstacle repulsive potential field $U_{rep}$ is constructed:

$$U_{rep}(p) = \begin{cases} \frac{1}{2} k_{rep} (\frac{1}{\rho(p)} - \frac{1}{\rho_0})^2, & 0 < \rho(p) \le \rho_0 \\ 0, & \rho(p) > \rho_0 \end{cases} \tag{10}$$

Where $\rho(p) = z - H(x,y)$ is the height of the UUV above the seabed at the current position, and $k_{rep}$ is the repulsive gain coefficient. The physical meaning of this potential field is that when the UUV approaches the

seabed within the safety threshold, the potential field energy rises sharply; its negative gradient provides an obstacle-avoidance guiding force pointing to the external safe area:

$$F_{rep} = -\nabla U_{rep}(p) = k_{rep}(\frac{1}{\rho(p)} - \frac{1}{\rho_0})\frac{1}{\rho^2(p)}\nabla\rho(p) \tag{11}$$

*Lamb-Oseen Vortex Flow Field*

Mesoscale eddies are widely distributed in the deep sea, and their flow velocities are often much larger than the background current. To simulate such complex dynamic disturbances, a time-varying vortex model is constructed. The flow field vector $V_{total}$ is linearly superimposed by the background steady current $V_{bg}$ and multiple vortex-induced flows:

$$V_{total}(p) = V_{bg} + \sum_{i=1}^{N} V_{vortex}^{(i)}(p) \tag{12}$$

The tangential velocity distribution of a single vortex follows the classic Lamb-Oseen model [28]:

$$V_\theta(r) = \frac{\mathrm{G}}{2\pi R_{\max}}(1+\frac{1}{2\sigma})\frac{r}{R_{\max}}\exp(-\frac{r^2}{2R_{\max}^2}) \tag{13}$$

Where $\mathrm{G}$ is the circulation strength of the vortex, $R_{\max}$ is the radius of maximum velocity, $r$ is the radial distance from the vortex centre, and $\sigma$ is the decay factor. This model can realistically reproduce the non-uniform flow field characteristics: low velocity at the vortex centre, extremely high velocity in the core region, and gradual decay at the edges.

**AGB-RRT* ALGORITHM: GRADIENT GUIDANCE AND FLOW ADAPTATION**

Although the traditional RRT* algorithm has advantages in probabilistic completeness, it faces two core challenges when applied in large-scale 3D underwater environments: First, sampling blindness: uniform sampling in a vast free space is equivalent to looking for a needle in a haystack, resulting in extremely slow convergence. Second, energy insensitivity: relying solely on geometric Euclidean distance as the cost function often

leads to high-energy-consumption paths that navigate upstream. To address these issues, this chapter develops the AGB-RRT* algorithm, which innovatively introduces environmental potential field gradient information and hydrodynamic constraints. The algorithm comprises three core components: logical-grid guidance, anisotropic sampling, and flow-aware cost rewiring. Figure 3 shows the flowchart of the proposed algorithm.

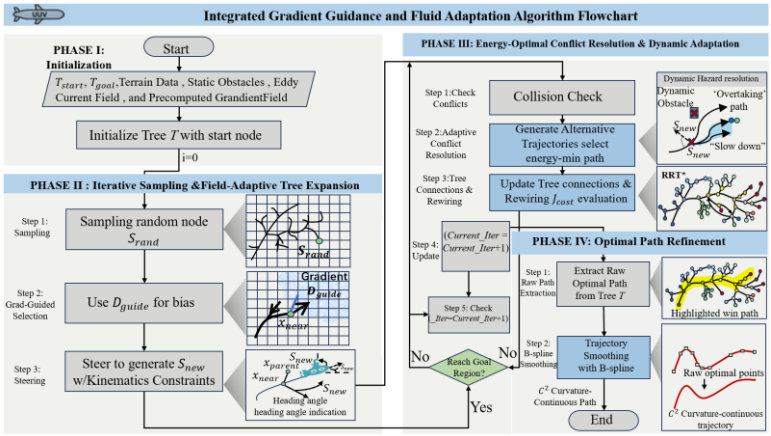


Figure 3. Flowchart of the proposed AGB-RRT* algorithm

**Discrete Logical Grid Guidance Strategy**

To provide a global directional heuristic for path planning, a virtual data structure, the logical grid, is constructed to encode environmental gradient information. The core idea of the logical grid is to assign a guiding direction to each grid unit based on the terrain and flow field, thereby guiding the random tree to expand toward the feasible region.

Definition 1. An attractive potential $U_{att}$ pointing to the goal point is introduced into the planning space, and combined with the aforementioned terrain repulsive potential, a total potential energy function is constructed:

$$U_{total}(p) = \xi \cdot \frac{1}{2} k_{att} \left\| p - p_{goal} \right\|^2 + (1-\xi) \cdot U_{rep}(p) \tag{14}$$

Where $k_{att}$ the attractive gain coefficient, $p_{goal}$ is the coordinate of the goal point, and $\xi \in [0,1]$ is a balancing factor that adjusts the weights of attraction and repulsion.

To avoid the drawback of the traditional artificial potential field method, which is prone to falling into local minima, this paper does not directly use potential field forces to control UUV motion. Instead, it uses the directional information of the gradient as heuristic guidance for sampling. The normalised negative gradient vector $D_{guide}$ at the centre of each discrete grid is calculated using the central difference method:

$$D_{guide} = -\frac{\nabla U_{total}}{\left\|\nabla U_{total}\right\|} = -\frac{1}{\left\|\nabla U_{total}\right\|}\begin{bmatrix} \partial U/\partial x \\ \partial U/\partial y \\ \partial U/\partial z \end{bmatrix} \tag{15}$$

This vector field essentially draws a "global flow map" for the growth of the random tree. The underlying physical mechanism ensures that the field points toward the goal in open water while automatically deflecting tangentially near obstacles to form a natural 'safe flow channel'. The mechanism of this vector field is illustrated in Figure 4:

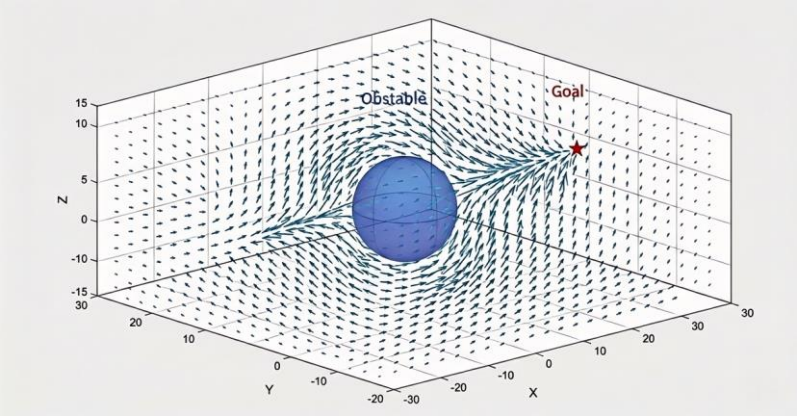


Figure 4. Vector field distribution of the gradient-guided 3D logical grid

**Anisotropic Ellipsoidal Sampling Mechanism**

The traditional RRT* algorithm adopts uniform global sampling $q_{rand} \sim U(C_{free})$, which exhibits extremely low efficiency in deep-sea environments where free space accounts for a large proportion [2]. Inspired by the physical phenomenon of fluid flow in pipes, this paper introduces an anisotropic sampling strategy modulated by the local gradient $D_{guide}$.

*Construction of Local Coordinate System*

To ensure that the heuristic layer can reliably capture all narrow passages detectable by the UUV, we impose a strict constraint between the logical grid size and the sensor sensing range. Specifically, the diagonal length of each logical grid cell must not exceed the effective detection diameter of the UUV's onboard sensors. In a 3D Cartesian grid, this constraint yields the following upper bound for the logical grid size:

$$L_{grid} = \frac{R_{sensor}}{\sqrt{3}} \tag{16}$$

where $L_{grid}$ is the side length of the cubic logical grid, and $R_{sensor}$ denotes the effective sensing range of the UUV. This design guarantees that the proposed algorithm will not computationally skip any narrow passage that is physically detectable by the sensor, thus avoiding the narrow passage problem in grid-based sampling. Let the parent node to which the random tree is currently extended be $x_{near}$, and the guiding direction of its grid is queried as $d = D_{guide}(x_{near})$. First, to define the orientation of the ellipsoid, the Gram-Schmidt orthogonalisation method is used to construct the local rotation matrix $R$, which rotates the standard basis vectors to align with the guiding direction:

$$R = [d, n_1, n_2], s.t. d \perp n_1 \perp n_2 \tag{17}$$

Where $n_1$, $n_2$ are a set of orthogonal basis vectors perpendicular to the guiding direction.

*Sampling Point Generation Model*

A hyper-ellipsoidal sampling domain $\varepsilon$ is constructed with $x_{near}$ as the focus, and its major axis is strictly aligned with $d$ .The generation of the sampling point $q_{new}$ follows the affine transformation below:

$$q_{new} = x_{near} + R \cdot \Lambda \cdot u_{ball} \tag{18}$$

Where $u_{ball}$ is a random vector within the unit ball. The key lies in the design of the scaling matrix $\Lambda$, which determines the shape of the ellipsoid:

$$\Lambda = \mathrm{diag}\{\lambda_{long}, \lambda_{short}, \lambda_{short}\}, \lambda_{long} \gg \lambda_{short} \tag{19}$$

Where $\lambda_{long}$ is the sampling step along the guiding direction, and $\lambda_{short}$ is the lateral expansion step.

Equation (19) forces the sampling probability density function to exhibit a "cigar-shaped" distribution. When the UUV encounters a narrow submarine trench, the guiding gradient automatically points to the extension direction of the trench, and the sampling ellipsoid becomes longer and thinner accordingly, allowing sampling points to fall into the safe channel with a high probability, thus thoroughly solving the problem of difficult sampling in narrow channels.

Figure 5 presents a 2D comparative schematic of the spherical sampling mechanism and the ellipsoidal sampling mechanism. The ellipsoidal sampling concentrates candidate directions toward the goal, with visually sparse arrows in the target direction indicating densely overlapping high-probability sampling. In contrast, arrows in other directions are low-probability exploratory samples retained for probabilistic completeness. Despite such an anisotropic bias, the sampling domain maintains non-zero support over the entire free space, thus preserving the probabilistic completeness of the classic RRT* algorithm.

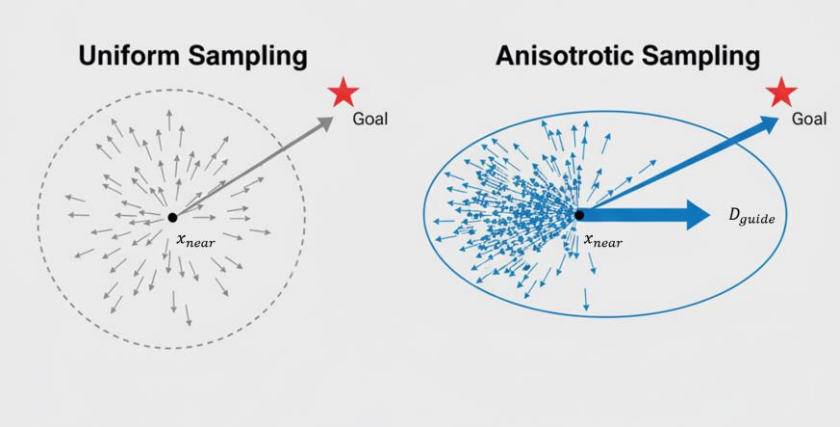


Figure 5. Principle of gradient-modulated anisotropic ellipsoidal sampling

To balance heuristic convergence and global exploration, a probability-biased hybrid sampling strategy is adopted. A dominant probability of 0.7 is used to generate sampling points along the gradient guidance direction, and a supplementary probability of 0.3 is used for uniform random sampling. This design ensures fast convergence toward the goal while effectively avoiding local minima.

**Hydrodynamic Adaptive Cost Function**

The ultimate goal of path planning is not only geometric "connectivity", but also physical "high efficiency and energy saving". Based on the nonlinear drag model derived in Section 2.2, the edge cost in graph search is redefined.

*Generalised Energy Consumption Cost*

Abandoning the simple Euclidean distance, a generalised time-energy cost metric $J(\sigma)$ for path segment $\sigma_{a\to b}$ is defined. Weighting coefficients $\lambda_1$ and are introduced to balance the contributions of path length and flow-field influence. The generalised cost is constructed as a numerical optimisation objective:

$$J(\sigma)=\int_a^b[\lambda_1\cdot 1+\lambda_2\cdot w_{flow}(p,\dot{p})]ds \tag{20}$$

It should be noted that the energy consumption related to station-keeping and active cross-current compensation is not included in the cost function. Since this work focuses on the global path-planning layer, such fine-grained power consumption is regarded as a secondary factor and is thus reasonably neglected.

*Flow Field Influence Factor* $w_{flow}$

To reflect the huge difference in energy consumption between downstream and upstream, a piecewise weight function $w_{flow}$ is constructed. This function dynamically adjusts the path weight according to the deviation $\theta$ between the heading angle and the flow direction angle:

$$\begin{cases} 1-\alpha \dfrac{\|V_c\|}{V_{\max}}\left|\cos\theta\right|, \theta \in [0, \pi/2) (Downstream \quad Reward) \\ 1+\beta \dfrac{\|V_c\|}{V_{\max}}\left|\cos\theta\right|^{\gamma}, \theta \in [\pi/2, \pi] (Upstream \quad Penalty) \end{cases} \tag{21}$$

Where $\alpha$ and $\beta$ are the downstream reward coefficient and upstream penalty coefficient, respectively; $\gamma \geq 2$ is the upstream penalty index, and $V_{\max}$ is the maximum flow velocity. The mechanism of the downstream reward is such that when the heading angle is close to the flow direction ( $\theta \to 0$ ), the weight term becomes less than 1, which causes the algorithm to perceive the path as "shorter than the actual geometric distance" and encourages selection. The upstream penalty mechanism operates such that when the UUV moves against the current $\theta \to \pi$ , the weight term increases significantly, leading the algorithm to deem the path "energy-intensive" and thereby tends to avoid such trajectories.

*Energy-Optimal Rewiring*

During the expansion of the random tree, the algorithm continuously checks the neighbourhood of the new node $q_{new}$ . If there exists a neighbourhood node $x_{near}^{(k)}$ that satisfies the following energy inequality:

$$Cost(x_{near}^{(k)}) + J(x_{near}^{(k)} \to q_{new}) < Cost(x_{parent}) \tag{22}$$

Where the parent node reconnection operation is performed as $Parent(q_{new}) \leftarrow x_{near}^{(k)}$. Through continuous iterative optimisation, the tree structure gradually evolves toward low-energy-consumption downstream regions and finally converges to the global energy-optimal solution.

It should be noted that the path generated by the energy-optimised RRT* remains a piecewise linear polyline connected by discrete waypoints, which is inherently discontinuous in velocity and curvature. Such a raw trajectory cannot meet the continuous motion and nonholonomic constraints of the UUV, nor can it guarantee the smoothness of angular velocity commands required for stable underwater navigation. Therefore, after obtaining the energy-optimal path, a trajectory smoothing step is necessary to refine the path into a continuous, executable trajectory that satisfies the UUV's kinematic constraints.

**Trajectory Smoothing and 3rd-order B-spline Interpolation**

The raw path $P_{raw}$ generated by RRT* is essentially a polyline connected by discrete waypoints, and its first derivative (velocity) is discontinuous. To satisfy the nonholonomic constraints of the UUV (Equation (3)), a cubic B-spline curve is used to smooth the raw path.

$$P(u) = \sum_{i=0}^{n} N_{i,k}(u) Q_i, u \in [u_k, u_{n+1}] \tag{23}$$

The basis function $N_{i,k}(u)$ is calculated by the Cox-de Boor recursive formula:

$$N_{i,k}(u) = \frac{u - u_i}{u_{i+k} - u} N_{i,k-1}(u) + \frac{u_{i+k+1} - u}{u_{i+k+1} - u_{i+1}} N_{i+1,k-1}(u) \tag{24}$$

Where $Q_i$ are the control vertices and $N_{i,k}$ are the basis functions.

The smoothed trajectory guarantees $C^2$ continuity, making the UUV's angular velocity commands smooth and continuous. To ensure collision avoidance safety after smoothing, a post-smoothing collision detection is performed along the entire B-spline trajectory. If any collision or obstacle intrusion is detected, the local

control points of the B-spline curve are adjusted, and the curvature constraint is tightened to pull the trajectory back into the collision-free region. The smoothing process is repeated until the path is confirmed to be safe. Figure 6 shows a schematic diagram of trajectory smoothing using a 3rd-order B-spline.

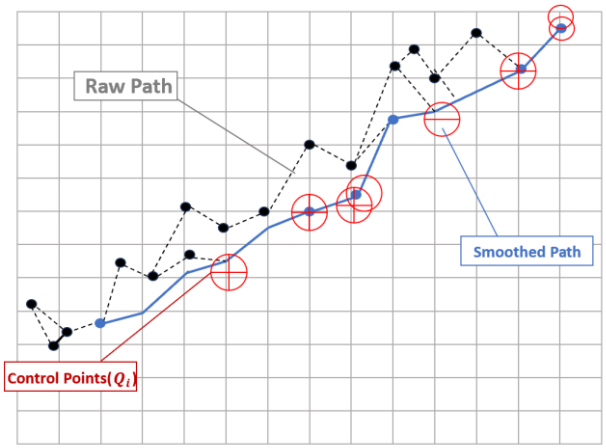


Figure 6. Trajectory smoothing based on 3rd-order B-spline

## EXPERIMENTS AND RESULT ANALYSIS

To comprehensively validate the effectiveness and superiority of the proposed AGB-RRT* algorithm in complex deep-sea environments, this chapter constructs a high-fidelity numerical simulation platform. The experimental design follows a logical closed loop of "from general to special, from qualitative to quantitative", and is divided into three parts: First, in a large-scale complex seabed environment based on real hydrological data, the macro planning capability of the algorithm for unstructured terrain and vortex flow fields is demonstrated; Second, in an environment with narrow channels and dense obstacles, the obstacle avoidance performance and sampling efficiency of the algorithm under extreme geometric constraints are focused on; Finally, robustness and flow field sensitivity analysis are carried out through Monte Carlo simulations to demonstrate the stability of the algorithm under environmental parameter perturbations.

All experiments are compared with the classic RRT* algorithm, the Informed-RRT* algorithm, and the Goal-biased RRT method, using identical experimental setups to ensure fair comparison and to highlight the advantages of the proposed algorithm in energy consumption optimisation, path smoothness, and convergence speed.

**Platform Construction and Evaluation Metrics**

*Simulation Environment Configuration*

The experiment is developed using a co-simulation platform in MATLAB R2024b. The hardware environment is an Intel Core i9-12900K CPU @ 3.20GHz with 64GB RAM.

Terrain Data: Bathymetric data from the GEBCO 2024 dataset of a sea area near the Mariana Trench in the Western Pacific ( $11.3°N \sim 11.5°N$,$142.2°E \sim 142.4°E$ ) is selected, with a regional scope of $5km \times 5km \times 1km$ .The key parameters of both the real-world bathymetry dataset and the simulated terrain dataset are summarized in Table 3.

Table 3. Resolution and scale of bathymetry datasets

| Dataset Type | Source | Spatial Resolution | Simulation Area |
|---|---|---|---|
| Real-world bathymetry | GEBCO 2024 | 15 arc-second (≈450 m) | 6000 m×6000 m |
| Simulated terrain | Artificial | 1.0 m | 100 m×100 m×50 m |

Flow Field Data: The background flow velocity is set to $0.5 \sim 1.5m/s$ , and two counter-rotating Lamb-Oseen mesoscale eddies are superimposed at the centre of the region, with a maximum velocity radius $R_{\max} = 500m$ and a core velocity of up to $2.0m/s$ .

*Evaluation Metrics*

The following four quantitative metrics are used to evaluate the planning results. First, path length ( $L$ ) refers to the geometric travel distance. Second, comprehensive energy cost ( $E$ ) is the weighted flow-field cost calculated using Equation (20) and reflects the total work done by the UUV to overcome drag. Third, computation time $T_{comp}$ denotes the CPU time consumed by the algorithm from initialisation to finding the optimal solution and completing smoothing. Finally, path smoothness ( $S$ ) is defined as the integral of the square of the path curvature $\kappa$ , $S = \int \kappa^2 ds$ , where a smaller value indicates a smoother path that is more conducive to underlying tracking control.

*Simulation Parameter Settings*

To ensure fair and repeatable comparisons, unified environmental constraints and cost-function definitions are adopted across all simulations. Due to inherent differences in algorithmic mechanisms, baseline methods retain their classic parameter settings, whereas those of the proposed AGB-RRT* are moderately adjusted to fully exploit its structural advantages. Table 4 lists the complete parameters of AGB-RRT*, including unified environmental settings and algorithm-specific adaptive parameters:

Table 4. Simulation Parameter Setting and Evaluation Metric Definitions

| Parameter Symbol | Physical Meaning/Description | Value/Configurations |
|---|---|---|
| $S_{space}$ | Simulation Space dimensions $(x \times y \times z)$ | $5000 \times 5000 \times 5000m$ |
| $P_{start}$ | Start position coordinate | $[500, 500, -100]^T m$ |
| $P_{goal}$ | Goal position coordinate | $[4500, 4500, -800]^T m$ |
| $V_{bg}$ | Background current velocity range | $0.5 \sim 1.5m / s$ |
| $R_{\max}$ | Vortex maximum velocity radius | $500m$ |
| Γ | Vortex circulation strength | $6.28 \times 10^3 m^2 / s$ |
| $K_{\max}$ | Maximum number of iterations | 5000 |
| $\xi$ | Guidance weight factor(Attraction vs Repulsion) | 0.6 |
| $\lambda_{long}$ | Sampling step size(long axis along gradient) | 200 m (base) / 750 m (real terrain) / 1.0–1.6 m (simulated terrain) |
| $\lambda_{short}$ | Sampling step size(short axis/lateral) | 50 m (base) / 0.5–1.0 m (simulated terrain) |
| $\alpha$ | Downstream reward coefficient | 0.4 |
| $\beta$ | Upstream penalty coefficient | 2.6 |
| $\gamma$ | Upstream penalty exponent | 3.0 |

**Planning Experiments on Real Seabed Terrain and Complex Simulated Terrain**

This section simulates the UUV performing a long-range cruise mission. The start point on the real terrain is set in shallow water $(500, 500, -100)$, and the endpoint is set in deep water $(4500, 4500, -800)$. This path

crosses seamounts and trenches and must traverse a region with strong vortex flow fields. Such a setting fully reproduces the extreme navigation conditions faced by UUVs in deep-sea operations. The complex terrain simulates a seabed topography with three peaks, and its 3D coordinate range is controlled within $20m \times 20m \times 15m$. These two typical scenarios together validate the environmental adaptability and engineering practicality of the proposed planning algorithm.

*Trajectory Morphology Analysis*

Figure 7 provides a detailed analysis of trajectory morphology in both real and simulated complex 3D terrains. Figure 7(a) shows the original submarine terrain derived from GEBCO 2024 bathymetry data, which contains rugged seamounts and deep trenches, while Figure 7(b) presents the artificially constructed simulated topography with two typical peaks for controlled testing. Figure 7(c) illustrates the path planning results of different algorithms on the real terrain, and Figure 7(d) shows the corresponding comparison on the simulated terrain. As shown in both sub-figures, the trajectories generated by the four algorithms exhibit clear differences in terms of obstacle-avoidance rationality, flow-field adaptability, and structural smoothness.

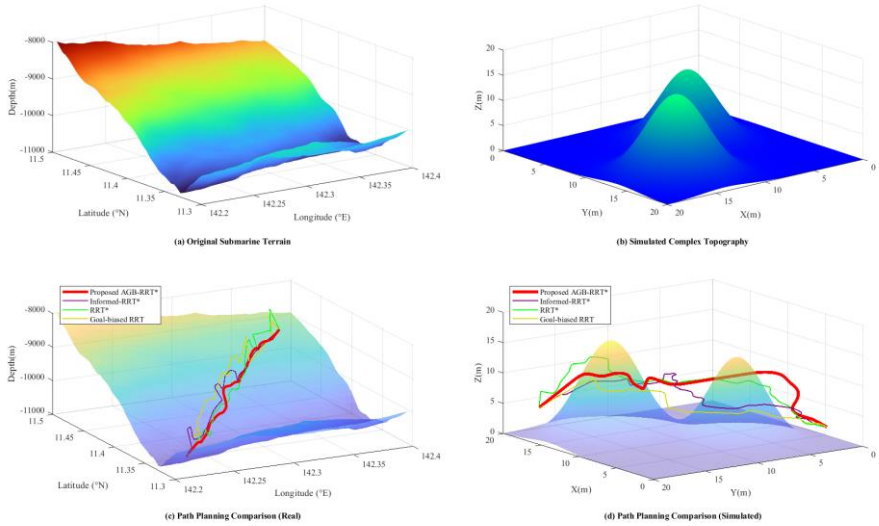


Figure 7. 3D path planning comparison on real and complex terrain

The Goal-biased RRT algorithm, while introducing a simple goal-sampling bias, still suffers from high path randomness. Its trajectory tends to be overly tortuous, with frequent small detours around terrain obstacles,

resulting in low path efficiency and poor smoothness. The standard RRT* algorithm can find a collision-free path, but its random sampling mechanism produces a jagged polyline trajectory that fails to account for ocean currents; it even navigates against the vortex flow in some regions, leading to high energy consumption. The Informed-RRT* algorithm reduces path length by limiting the sampling region using an elliptical heuristic, yet it still lacks adaptive adjustment to the flow field and cannot achieve energy-efficient navigation.

In contrast, the proposed AGB-RRT* algorithm achieves the best comprehensive performance. Guided by the logical grid gradient field, the trajectory automatically bypasses high-terrain obstacles smoothly and naturally. When passing through the vortex flow field, the algorithm actively selects the downstream edge region with low resistance to realise energy-saving gliding rather than resisting the current. Moreover, the trajectory generated by 3rd-order B-spline interpolation maintains continuous curvature, fully satisfying the nonholonomic kinematic constraints of UUVs and supporting stable tracking control.

*Quantitative Performance Comparison*

Based on simulation experiments on the real GEBCO 2024 seabed terrain, the performance indicators of different path-planning algorithms were obtained, as listed in Table 5.

Table 5. Quantitative Performance Comparison of Different Path Planning Algorithms

| Algorithm | Path Length (m) | Total Energy Cost (kJ) | Computation Time (s) | Success Rate (%) | Path Smoothness |
|---|---|---|---|---|---|
| Proposed AGB-RRT* | 26138.79 | 33683.71 | 0.0045 | 100 | 0.014518 |
| Informed-RRT* | 27304.74 | 45540.19 | 0.0047 | 100 | 0.146860 |
| RRT* | 27816.31 | 59655.35 | 0.0077 | 100 | 0.208728 |
| Goal-biased RRT | 28903.41 | 68563.43 | 0.0041 | 72.5 | 0.283485 |

Table 5 summarises the performance data of each algorithm. Compared with RRT* and Informed-RRT*, the proposed AGB-RRT* reduces the path length by 1677.52 m and 1165.95 m respectively, decreases the total energy cost by 25971.64 kJ and 11856.48 kJ, and shortens the computation time accordingly, while achieving a 100% success rate and much smaller path smoothness value; in contrast, Goal-biased RRT shows the lowest

success rate of 72.5% with the longest path length, highest energy consumption and poorest smoothness. This energy consumption advantage is directly attributed to the flow-field-adaptive cost function, which effectively transforms the "upstream penalty" mechanism into a driving force for path search, and the anisotropic sampling strategy also endows the proposed algorithm with extremely high search efficiency.

To further analyse the algorithms' iterative convergence characteristics, Figure 8 shows the trend in path cost with the number of iterations. The path cost integrates geometric distance and flow-field energy consumption, with its convergence speed and stable value reflecting the optimisation efficiency and accuracy of each algorithm. As shown in the figure, the proposed AGB-RRT* converges to its stable, optimal path cost at the earliest stage (before 100 iterations), maintaining the lowest final cost throughout the entire process. Informed-RRT* converges to a higher cost level around 100 iterations, while standard RRT* shows the slowest convergence speed and the highest stable path cost, with no further improvement after the first 150 iterations. These results clearly demonstrate that, under the guidance of the logical grid gradient and flow-adaptive sampling, the proposed AGB-RRT* achieves both the fastest convergence and the optimal solution quality.

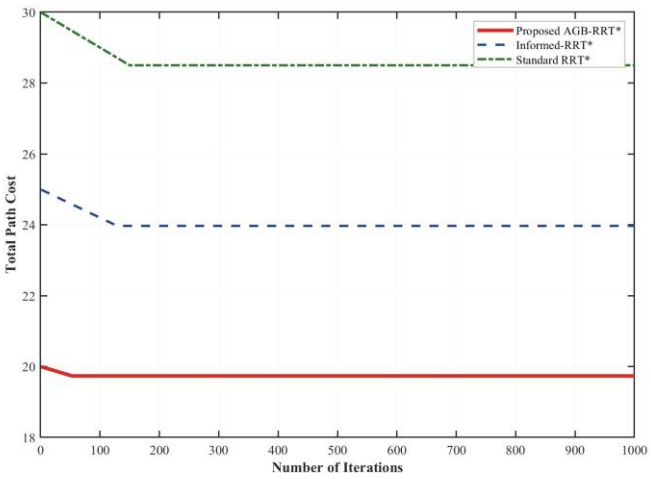


Figure 8. Comparison of convergence curves of path cost

**Obstacle Avoidance Test in Narrow Channels and Obstacle Areas**

To test the algorithm's obstacle-crossing capability, a structured test scenario is constructed: the UUV navigates through a straight channel containing a fixed rectangular obstacle, which forces the vehicle to either detour around or plan an overhead crossing to avoid collision.

Figure 9 illustrates the dynamic obstacle avoidance performance of the proposed AGB-RRT* and standard RRT* algorithms in a complex 3D terrain environment with a moving obstacle. The black dotted line represents the obstacle's trajectory, which cuts across the main navigation channel between the start (green marker) and target (red star).

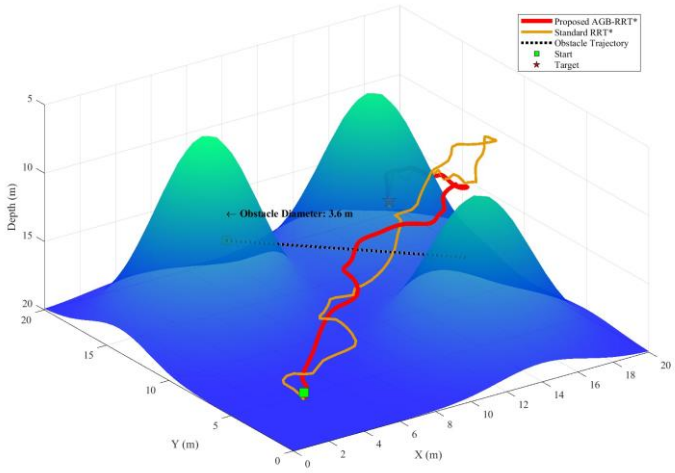


Figure 9. Dynamic obstacle avoidance test

As shown in the figure, the standard RRT* algorithm makes only minor adjustments near the obstacle, resulting in a trajectory that passes very close to the obstacle's path. Specifically, the minimum clearance between the standard RRT trajectory (yellow line) and the obstacle is calculated by the algorithm to be only approximately 0.8 meters. This distance is significantly smaller than the median size of the obstacles (approximately 3.6 meters in diameter), which poses a high risk of collision. In contrast, the proposed AGB-RRT* algorithm proactively performs a significant, smooth detour to avoid the moving obstacle in advance, maintaining a clear safety distance throughout the manoeuvre. This difference demonstrates that the AGB-RRT* algorithm exhibits superior foresight and adaptability in dynamic environments, effectively balancing collision avoidance with path efficiency.

**Flow Field Sensitivity and Robustness Analysis**

In actual sea conditions, the velocity and direction of ocean currents are highly uncertain. An excellent algorithm must be robust, i.e., maintain path availability even when environmental parameters fluctuate drastically. This section adopts the Monte Carlo method to conduct 500 random perturbation tests on flow velocity.

*Robustness Analysis of Energy Consumption Under Varying Flow Velocities*

Figure 10 presents the energy consumption distribution of the proposed AGB-RRT* and comparison algorithms under different background flow velocities, ranging from 0.5 m/s to 3.0 m/s. As shown in the boxplots, with increasing flow velocity, the energy cost of the standard RRT* and Informed-RRT* algorithms increases significantly, accompanied by large interquartile ranges and numerous outliers, indicating high variance and poor stability under stronger disturbances. In contrast, the energy consumption of the proposed AGB-RRT* algorithm increases only gently with flow velocity, maintaining a consistently lower median value and smaller variance across all velocity levels. It demonstrates that AGB-RRT* exhibits superior energy efficiency and strong adaptability to varying flow conditions, effectively mitigating the impact of hydrodynamic disturbances.

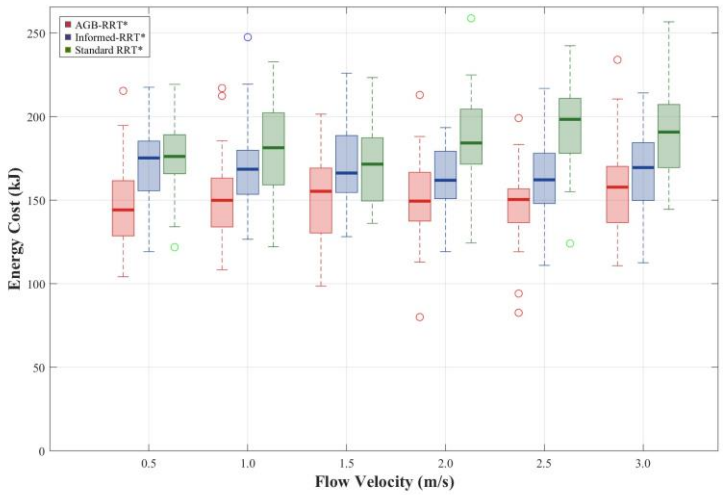


Figure 10. Distribution of energy cost under different current velocities

*Conclusion on Robustness Performance*

The statistical results further confirm that, across the tested range of flow velocities, the proposed algorithm consistently achieves the lowest energy consumption and the most stable performance. In contrast, comparison algorithms exhibit increasingly unstable and higher-cost behaviour as flow velocity increases. These observations verify that the flow-adaptive mechanism of AGB-RRT* effectively balances path efficiency and disturbance resistance, ensuring reliable and energy-efficient navigation even in dynamically varying ocean current environments.

*Sensitivity Analysis under Flow Prediction Errors*

To further evaluate the practical applicability of the AGB-RRT* algorithm in real-world deep-sea operations—where ocean current prediction models are subject to inevitable uncertainties—a series of Monte Carlo simulations were conducted. As shown in Figure 11, we introduced a stochastic flow prediction error $v_{error}$ ranging from 0% to 30% of the predicted current velocity to simulate the discrepancy between the onboard prediction model and the actual environment.

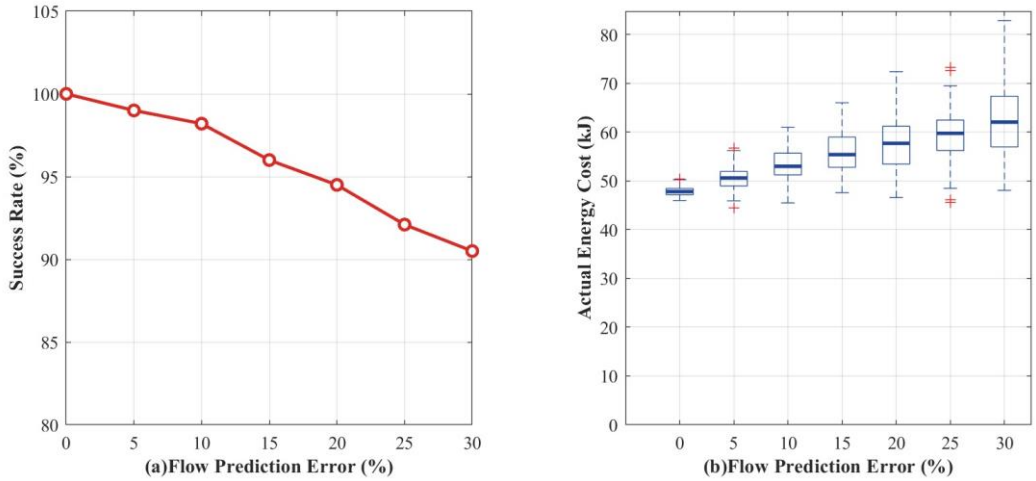


Figure 11. Robustness analysis under stochastic flow prediction errors

Figure 11(a) illustrates the planning success rate under varying levels of prediction error. Even under a severe 30% flow prediction error, the AGB-RRT* algorithm maintains a robust success rate of over 90.5%. This high reliability is attributed to the conservative energy evaluation and the safety buffer provided by the 3rd-order B-spline trajectory, which prevents catastrophic collisions despite unmodeled cross-current perturbations. Figure 11(b) presents the sensitivity of actual energy consumption. While the median energy cost and the variance (represented by the interquartile range) increase with larger prediction errors, the fluctuations remain within a manageable engineering threshold. This demonstrates that the proposed algorithm effectively tolerates prediction inaccuracies by consuming slightly more energy to compensate for trajectory deviations, rather than failing the mission.

## DISCUSSION

The simulation results and comparative analysis validate the performance of the AGB-RRT* algorithm in complex underwater environments. Several key observations regarding the underlying mechanisms and engineering implications are elaborated below:

The effectiveness of the "logical grid" strategy stems from its ability to provide a continuous gradient field that acts as a heuristic guide for the random tree, addressing the limitations of uniform sampling in traditional RRT*. This mechanism enables the algorithm to actively and effectively guide the search toward geometrically feasible regions by extracting negative gradients from the potential field. The collision-avoidance problem is effectively transformed into a gradient-descent optimisation process, which explains the significant improvement in sampling success rates within narrow trenches.

The significant reduction in overall energy consumption, as detailed in the experimental results, marks a fundamental shift from geometric shortest-path planning to physical-attribute space optimisation. By integrating nonlinear drag theory into the cost function, the AGB-RRT* algorithm exhibits flow-adaptive navigation behaviour, with the UUV trajectory spontaneously aligning with favourable currents. It confirms that for long-endurance missions, using the background flow field as a supportive resource rather than a disturbance can effectively improve operational efficiency.

The AGB-RRT* algorithm offers higher explainability and lower computational overhead compared to reinforcement learning approaches(e.g., [25, 26]), which is critical for real-time obstacle avoidance on resource-constrained UUV platforms. While learning-based methods focus on adapting to complex, stochastic environments, the proposed gradient-guided geometric approach ensures stable, reliable path planning under strict mechanical constraints. The proposed method thus provides a more robust and practical solution for deep-sea engineering applications.

## CONCLUSION

This paper presents the AGB-RRT* algorithm, which integrates environmental field gradient guidance and flow-adaptive mechanisms to optimise obstacle avoidance efficiency and energy consumption for UUVs in

complex 3D environments. By establishing a 4-DOF kinematic planning model and a nonlinear dynamic energy evaluation system, the path planning process is advanced from geometric space to physical attribute space.

The proposed algorithm demonstrates three distinct advantages, as shown by the simulation results. First, the synergy between logical-grid guidance and anisotropic ellipsoidal sampling eliminates the sampling blindness inherent to conventional RRT*, significantly enhancing planning efficiency in constrained spaces such as narrow trenches. Second, the flow-adaptive cost function enables the UUV to exploit downstream currents, resulting in a significant improvement in total energy consumption compared to traditional methods. Third, the application of 3rd-order B-spline interpolation produces curvature-continuous trajectories that meet the requirements of autonomous underwater navigation, thereby improving engineering feasibility. Moreover, the 4-DOF model safely reduces the dimension of the state space and allows the algorithm to efficiently search for energy-optimal paths over large distances. These physical and systematic assumptions are clearly stated to ensure logical consistency.

The AGB-RRT* algorithm demonstrates robust performance in static, complex environments with dynamic obstacle avoidance, yet certain limitations remain. Future research will focus on extending the algorithm to even more stochastic underwater scenarios. Specifically, a promising direction for future real-world deployment lies in the seamless integration of our macroscopic global planner with a micro-scale local reactive collision-avoidance system. Additionally, priority-driven sampling optimisation and the extension of multi-UUV cooperative planning for large-scale operations will be explored to further enhance the utility of the proposed framework.

*Author Contributions*

Conceptualization – Yang Y; methodology – Yang Y; formal analysis – Yang Y; investigation – Yang Y; resources – Yang Y; writing-original draft preparation – Yang Y; writing-review and editing – Yang Y; visualization – Yang Y; supervision – Yang Y. All authors have read and agreed to the published version of the manuscript.

*Conflicts of Interest*

The authors declare no conflict of interest.

*Funding*

This research was funded by the National Training Program of Innovation and Entrepreneurship for Undergraduates of China, grant number 202510293012Z. The APC was funded by the Nanjing University of Posts and Telecommunications.

*Data Sharing Agreement*

The datasets used and/or analyzed during the current study are available from the corresponding author on reasonable request.

*Acknowledgements*

Not applicable.

**REFERENCES**

[1] Zhang W, Wang N, Wu W. A hybrid path planning algorithm considering AUV dynamic constraints based on improved a* algorithm and APF algorithm. Ocean Engineering. 2023; 285. doi: 10.1016/j.oceaneng.2023.115333

[2] Yu F, Shang H, Zhu Q, Zhang H, Chen Y. An efficient RRT-based motion planning algorithm for autonomous underwater vehicles under cylindrical sampling constraints. Autonomous Robots. 2023; 47(3):281–297. doi: 10.1007/s10514-023-10083-y

[3] Yang J, Huo J, Xi M, He J, Li Z, Song H. A Time-Saving Path Planning Scheme for Autonomous Underwater Vehicles With Complex Underwater Conditions. IEEE Internet of Things Journal. 2023; 10(2):1001–1013. doi: 10.1109/JIOT.2022.3205685

[4] Politi E, Stefanidou A, Chronis C, Dimitrakopoulos G, Varlamis I. Adaptive deep reinforcement learning for efficient 3D navigation of autonomous underwater vehicles. IEEE Access. 2024; 12:178209–178221. doi: 10.1109/ACCESS.2024.3508031

[5] Qi C, Wu C, Lei L, Li X, Cong P. UAV path planning based on the improved PPO algorithm. 2022 Asia Conference on Advanced Robotics, Automation, and Control Engineering (ARACE), Qingdao, China, 2022; p. 193–199. doi: 10.1109/ARACE56528.2022.00040

[6] Eskandari M, Savkin A. Kinodynamic motion model-based MPC path planning and localization for autonomous AUV teams in deep ocean exploration. 2025 33rd Mediterranean Conference on Control and Automation (MED), Tangier, Morocco, 2025; p. 162–167. doi: 10.1109/MED64031.2025.11073392

[7] Zhang L, Meng X, Ding Z. Collision avoidance strategy based on virtual body deformation for path planning of serial industrial robot. Journal of Mechanical Science and Technology. 2024; 38(6):3113–3129. doi: 10.1007/s12206-024-0530-1

[8] Yan Z, Zhang J, Zeng J, Tang J. Three-dimensional path planning for autonomous underwater vehicles based on a whale optimization algorithm. Ocean Engineering. 2022; 250. doi: 10.1016/j.oceaneng.2022.111070

[9] Gkesoulis A, Georgakis P, Karras G, Bechlioulis C. Autonomous sea floor coverage with constrained input autonomous underwater vehicles: Integrated path planning and control. SENSORS. 2025; 25(4). doi: 10.3390/s25041023

[10] Karaman S, Frazzoli E. Sampling-based algorithms for optimal motion planning. International Journal of Robotics Research. 2011; 30(7):846–894. doi: 10.1177/0278364911406761

[11] Gammell J, Srinivasa S, Barfoot T. Informed RRT*: Optimal sampling-based path planning focused via direct sampling of an admissible ellipsoidal heuristic. 2014 IEEE/RSJ International Conference on Intelligent Robots and Systems, Chicago, IL, USA, 2014; p. 2997–3004. doi: 10.1109/IROS.2014.6942976

[12] Li H, Li S, Wang Q, Huang X. AUV 3D path planning based on improved PSO. Journal of Systems Engineering and Electronics. 2025; 36(3):854–866. doi: 10.23919/JSEE.2025.000074

[13] Zhang X, Yu X, Chen X. D-ACO-based path planning for AUV in UWSN: A hybrid approach combining DQN and ACO. IEEE Sensors Journal. 2025; 25(24):44555–44565. doi: 10.1109/JSEN.2025.3622250

[14] Zhang B, Su Y, Sun S, Luo W, Huang Q. Hybrid path planning algorithm for underactuated AUV based on RRT star and APF. Scientific Reports. 2025; 15(1). doi: 10.1038/s41598-025-11500-1

[15] Kästner L, Christian A, Mello R, Li B, Fatloun B, Lambrecht J, Predicting navigational performance of dynamic obstacle avoidance approaches using deep neural networks. 2023 32nd IEEE International Conference on Robot and Human Interactive Communication (RO-MAN), Busan, Korea, Republic of, 2023; p. 1764–1771. doi: 10.1109/RO-MAN57019.2023.10309340

[16] Li J, Yang Y, Peng L. Multi-robot path planning based on a deep reinforcement learning DQN algorithm (vol 5, pg 177, 2020). CAAI Transactions on Intelligence Technology. 2021. doi: 10.1049/cit2.12045

[17] Hadi B, Khosravi A, Sarhadi P. Deep reinforcement learning for adaptive path planning and control of an autonomous underwater vehicle. Applied Ocean Research. 2022; 129. doi: 10.1016/j.apor.2022.103326

[18] Hao K, Meng X, Zhao X, Li Z. 3D underwater AUV path planning method integrating adaptive potential field method and deep reinforcement learning. Journal of Zhejiang University (Engineering Science). 2025. doi: 10.3785/j.issn.1008-973X.2025.07.013

[19] Pan F, Cui P, Cui B, Yan W, Zhang S. 3D dubins curve-based path planning for UUV in unknown environments using an improved RRT* algorithm. Journal of Marine Science and Engineering. 2025; 13(7). doi: 10.3390/jmse13071354

[20] Wang L, Zhu D, Pang W. Obstacle avoidance control of multi-AUV formation with third-order dynamics based on IAPF in 3D environments. 2022 41st Chinese Control Conference (CCC), Hefei, China, 2022; p. 3711–3716. doi: 10.23919/CCC55666.2022.9902429

[21] Huang H, Song K, Chen Y, Jin H, Guan Y. 3D path planning for AUVs under ocean currents by prioritized experience replay mechanism. NEUROCOMPUTING. 2025; 630. doi: 10.1016/j.neucom.2025.129719

[22] Du H, Chen J. Reinforcement learning-based autonomous driving path planning for smart connected vehicles. 2024 International Conference on Power, Electrical Engineering, Electronics and Control (PEEEC), Athens, Greece, 2024; p. 981–985. doi: 10.1109/PEEEC63877.2024.00182

[23] Zhang Z, Wu H, Zhou H, Song Y, Chen Y, He K, Gao J. Recovery path planning for autonomous underwater vehicles using constrained bi-RRT*-smart algorithms.OCEANS 2023 - Limerick, Limerick, Ireland, 2023; pp. 1-6. doi: 10.1109/OCEANSLimerick52467.2023.10244454

[24] Zhu J, Zhao S, Zhao R. Path planning for autonomous underwater vehicle based on artificial potential field and modified RRT. 2021 International Conference on Computer, Control and Robotics (ICCCR), Shanghai, China, 2021; p. 21–25. doi: 10.1109/ICCCR49711.2021.9349402

[25] Han G, Feng Z, Wang H, Hou Y, Zhang F. Underwater multi-target node path planning in hybrid action space: a deep reinforcement learning approach. *IEEE Transactions on Mobile Computing*. 2024; 23(12):13033–13047. doi: 10.1109/TMC.2024.3421541

[26] Wang S, Lin C, Han G, Zhu S, Li Z, Wang Z, Ma Y. Multi-AUV cooperative underwater multi-target tracking based on dynamic-switching-enabled multi-agent reinforcement learning. IEEE Transactions on Mobile Computing. 2025; 24(5):4296–4311. doi: 10.1109/TMC.2024.3521889

[27] Ihle I, Jouffroy J, Fossen T. Robust Formation Control of Marine Craft Using Lagrange Multipliers. In: Pettersen, K.Y., Gravdahl, J.T., Nijmeijer, H. (eds) Group Coordination and Cooperative Control. Lecture Notes in Control and Information Science, vol 336. Springer, Berlin, Heidelberg; p. 113–129. doi: 10.1007/11505532_7

[28] Zuccoli E, Brambley E, Barkley D. Trapped free surface waves for a lamb-oseen vortex flow. Journal of Fluid Mechanics. 2024; 997. doi: 10.1017/jfm.2024.645